PHYSICAL REVIEW B **100**, 115307 (2019)

Incommensurate grain boundary in silicon and the silver-ratio sequence

Frédéric Lançon,[1,*] Nina Gunkelmann,[1,2] Damien Caliste,[1] and Jean-Luc Rouvière[3,†]
[1] *Université Grenoble Alpes, CEA, MEM, L_Sim, F-38000 Grenoble, France*
[2] *Institute of Applied Mechanics, Technische Universität Clausthal, Arnold-Sommerfeld-Straße 6, D-38678 Clausthal-Zellerfeld, Germany*
[3] *Université Grenoble Alpes, CEA, MEM, Lemma, F-38000 Grenoble, France*

(Received 13 March 2019; published 5 September 2019)

A scheme is proposed to solve the structure of incommensurate interfaces, starting from high-resolution images of electron microscopy, supplemented by adapted simulation techniques, and complemented by theoretical tools. Direct silicon bonding is a way to produce artificial interfaces, in particular incommensurate ones. We focus on a technology-driven tilt grain boundary in silicon. While the Fibonacci sequence, linked to the golden ratio, is a prototype of the quasicrystalline structures, a silver-ratio sequence allows us to analyze this incommensurate interface. The fourfold coordination of the Si atoms is kept at the interface.

DOI: 10.1103/PhysRevB.100.115307

I. INTRODUCTION

Direct wafer bonding [1,2] is a pathway to produce grain boundaries that may not occur naturally. In particular, attractive structures for semiconductor technology can be produced by bonding together a Si{011} wafer and a Si{100} one, with the [001] direction of the first wafer aligned with the [110] direction of the second one [3–7]. Indeed, in this system with mixed orientations, the hole mobility and the electron mobility have opposite enhancement in the wafers, leading to important technological advancements [8].

However, the resulting 90°⟨1 1 0⟩ tilt boundaries are incommensurate, since the two aligned directions [001] and [110] have periodicities with a ratio $\sqrt{2}$ between them. Because of this lack of periodicity of the grain boundaries, solving their atomic structures is not simple, though necessary to fully understand their properties. Several attempts have already been conducted [5,9], but without considering their incommensurate nature.

Although more complex than the periodic cases, the theoretical background to describe incommensurate grain boundaries was quickly provided as an extension of the quasicrystal understanding [10–15]. However, nowadays, high-resolution electron microscopes, as well as mature and precise simulation techniques [16–18], can be pursued to give accurate characterizations and quantitative analyses of the incommensurate grain boundaries.

In this work, we focus on the 90° ⟨1 1 0⟩ tilt boundary, but the approach is general to incommensurate interfaces in covalent materials. Our purpose is not to completely explain the atomic structure of the 90° ⟨1 1 0⟩ tilt grain boundary by energy considerations [19], but rather to extract the local atomic structures from high-resolution experiments. Indeed, through pattern matching, the characteristics of the interface are highlighted and two-dimensional coordinates are extracted. In principle, for a nonperiodic interface, a large area of the material should be analyzed to determine the subtle crystalline-site distortions at the interface. In our case however, two elemental units can be selected and arranged to produce infinite sequences relative to the silver ratio $1 + \sqrt{2}$, thanks to the quasicrystalline framework (see Sec. VII). From the 2D coordinates extracted from the experimental images of these units, we introduce a two-step energy minimization to retrieve the tridimensional atomic coordinates of the interface elements (see Sec. V). The atomic structures are then refined by nowadays precise DFT calculations (density functional theory).

Finally a complete atomic description of this incommensurate grain boundary in silicon is given. Note that a similar but metallic incommensurate boundary has been described with the same level of details [20]. However, we address here a different class of incommensurate grain boundaries where the structural unit model [14,15] is well adapted to describe them.

II. GRAIN-BOUNDARY DESCRIPTION

A 90° ⟨1 1 0⟩ tilt grain boundary in a cubic material is an interface between two crystalline grains having a common crystallographic direction ⟨1 1 0⟩ but where one grain is rotated by 90° with respect to the other one, around this common axis. Because the cubic cell of side a is projected into a rectangle of sides a and $\sqrt{2}a$ onto a {1 1 0} plane, the two grains have no coincidence site lattice in this plane. If there was one, the site coordinates of this lattice expressed respectively in both 2D rectangular cells would imply relations $na = m\sqrt{2}a$ with n and m being integers. The grain boundary is thus called incommensurate.

The orientation of the boundary itself is fixed by the grain bonding. In this study, the interface is parallel to the common axis and to one of the sides of the 2D rectangular cells (see Fig. 1). More precisely, $[1\,\bar{1}\,0]$ is the common axis of the two grains and taken as our z axis. This axis is therefore a

---

[*] Frederic.Lancon@cea.fr
[†] Jean-Luc.Rouviere@cea.fr

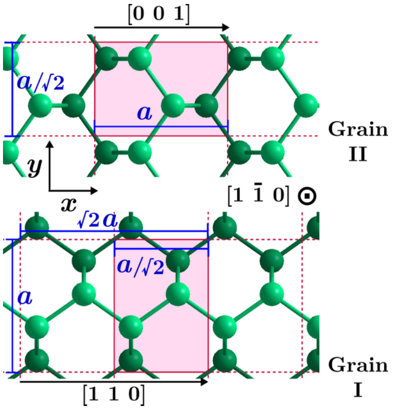

FIG. 1. Crystalline grain orientations on both side of the grain boundary. The Miller indices are relative to the cubic cell. The plan view is perpendicular to [1 $\bar{1}$ 0], which is the common direction of both grains (z axes here). The shades of the spheres indicate their altitude $z = 0$ or $z = a/(2\sqrt{2})$. The light-shade rectangles of sides a and $a/\sqrt{2}$ represent the silicon orthorhombic cells with the lattice vectors corresponding to [001], [110], and [1 $\bar{1}$ 0]. The *cubic* cell is projected onto (1 $\bar{1}$ 0) as a rectangle of sides a (side of the cube) and $\sqrt{2}a$ (diagonal of the face). The vector [001] of one of the crystal is parallel to the vector [110] of the other one, and thus the grain boundary is incommensurate. In this study, the interface is parallel to the xz plane.

commensurate direction of the interface. The interface contains the [110] direction of one grain, let's say grain I, and thus contains the [001] direction of grain II. This direction is the incommensurate direction of the interface and is chosen to be our x axis. The y axes is perpendicular to the interface.

III. APPROXIMANTS

The periods of grains I and II along the incommensurate direction (x) are denoted s and ℓ, respectively (s for short and ℓ for long). Grains I and II are, respectively, the lower and upper grains in figure 1. In the ideal incommensurate grain boundary, $s = a/\sqrt{2}$ and $\ell = a$, where a is the cubic lattice parameter of silicon. However, the atomic configurations considered for computation usually correspond to periodic approximants of the incommensurate grain boundary. In the same way that a sequence of rational numbers n_s/n_ℓ can tend to an irrational number, a sequence of periodic approximants can approach better and better an incommensurate structure. In the context of this paper, a "$n_s : n_\ell$ approximant" is a periodic boundary where n_s periodic cells of grain I are facing n_ℓ cells of grain II. The best matches between the two grains are obtained when the ideal lengths $n_\ell\,\ell$ and $n_s\,s$ have close values. This corresponds precisely to the strong condition to be verified by n_s and n_ℓ for n_s/n_ℓ to be among the best rational approximations of the ideal value of ℓ/s, i.e., $\sqrt{2}$ here:

$$\Delta[n_s, n_\ell] \equiv |n_\ell\sqrt{2} - n_s| < |q\sqrt{2} - p| \tag{1}$$

for any rational number p/q so long as $q < n_\ell$. With this condition, the best approximations are the continued-fraction convergents of $\sqrt{2}$. These convergents are 1/1, 3/2, 7/5, 17/12, and more generally $p_k/q_k = (2p_{k-1} + p_{k-2})/(2q_{k-1} + q_{k-2})$ at step $k > 2$. In our calculations, the period P of the $n_s : n_\ell$ approximant is the arithmetic mean of the corresponding ideal grain periods:

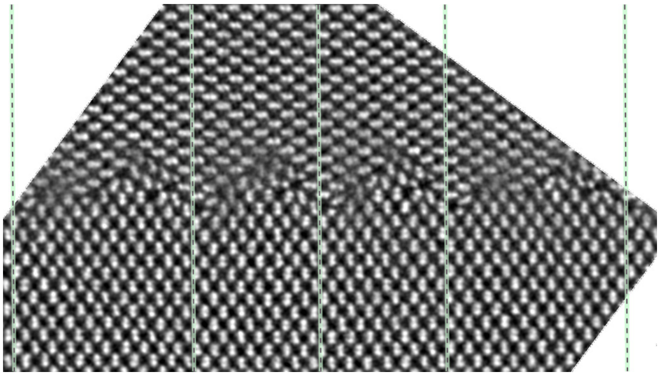

FIG. 2. Scanning transmission electron microscopy (STEM) image of the incommensurate grain boundary. Si atoms, individual or in adjacent pairs (dumbbells), are all resolved in this image. More precisely, each spot corresponds to an atomic column perpendicular to the plane view. Vertical lines indicate a possible decomposition into 7:5 and 10:7 approximants of the grain boundary (thinner and thicker strips, respectively). Note the good atomic match between atomic patterns at the different line locations making possible periodic boundary conditions for each approximant, or combinations of several 7:5 and 10:7 approximants.

$$P = a\,(n_\ell + n_s/\sqrt{2})/2. \tag{2}$$

The residual strains in grains I and II in the approximant are then respectively

$$\begin{aligned} \varepsilon_{x,I} &= (P - n_s s)/(n_s s) = \left(\frac{n_\ell}{n_s} - \frac{1}{\sqrt{2}}\right)/\sqrt{2}, \\ \varepsilon_{x,II} &= (P - n_\ell \ell)/(n_\ell \ell) = \left(\frac{n_s}{n_\ell} - \sqrt{2}\right)/(2\sqrt{2}) \\ &= -\varepsilon_{x,I} + \mathcal{O}\left(\left(\frac{n_s}{n_\ell} - \sqrt{2}\right)^2\right), \end{aligned} \tag{3}$$

and thus the minimal strains are also obtained by the best rational approximations n_s/n_ℓ of $\sqrt{2}$. Note that a convergent n_s/n_ℓ of $\sqrt{2}$ corresponds to the convergent n_ℓ/n_s of $1/\sqrt{2}$.

IV. ELECTRON MICROSCOPY RESULTS

Figure 2 is an electron-microscopy (STEM) image of the grain boundary observed along the common [1$\bar{1}$0] direction of the two grains. The experimental details are given in Ref. [5]. An atomistic model of the periodic 7:5 approximant of this grain boundary had already been proposed [5]. Indeed, a repeating pattern can be recognized with a pseudo periodicity corresponding to $n_s = 7$ periods of grain I and $n_\ell = 5$ periods of grain II. However, even if 7/5 is only 1 % smaller than $\sqrt{2}$, this would correspond to a tensile strain in grain I and a compressive strain in grain II of $\pm 5 \times 10^{-3}$ [Eq. (3)], impossible for the material to sustain macroscopically. In fact, a similar but longer pattern can also be identified in the microscopy images. It corresponds to a 10:7 approximant, i.e., $n_s = 10$ and $n_\ell = 7$. While 10/7 does not belong to the best approximations of $\sqrt{2}$, this approximant has about the same strain amount than the 7:5 one, but with an opposite sign for each grain. Thus, combining them together, as in figure 2, can reduce the strains to $\pm 9 \times 10^{-4}$. Indeed, $17/12 = (7 + 10)/(5 + 7)$ is the next best rational approximation after 7/5. In the following, we will consider the 7:5 and the 10:7 approximants as the structural units of the grain boundary. Their 3D structures will be solved by combining image analyses and numerical energy minimizations. The general way to combine them in a sequence of best approximants and thus to describe the infinite grain boundary will be discussed in Sec. VII.

V. FROM 2D TO 3D

A. Pattern recognition

The resolution of the experimental images is high enough to deduce with a good precision the x and y atomic coordinates of the Si atomic columns perpendicular to the image plane. To automatically extract a large number of coordinates, a pattern recognition technique [21] based on cross-correlation functions has been used. From the experimental image, three small portions representative of three material characteristics are selected: The individual atomic column and the two possible orientations of Si dumbbells composed of two columns. Three cross-correlation functions are first calculated between the image and each of the three templates. As described in Ref. [21], three smoother patterns are obtained by averaging image sections located at high correlation maximums (see Fig. 3). A second set of correlation functions is then calculated. Taking advantage of the three-dimensional nature of the color image coding, we introduce here a way to gather these three functions and get a direct visualization of the information. For all pixels, each color component red, green, or blue, is associated with the value of one of the cross-correlation functions. Figure 3 shows that the different constituents of the grain boundary are now clearly identified. Then, isolated columns, or pairs of them, are associated with Gaussian functions that are fitted on the initial image using the locations of the correlation maxima as initial guesses. To improve the recognition of the atom positions, the low intensity around each image spot was assigned to zero thanks to an apodization function. The 2D Si positions finally extracted from the experimental image are also shown in Fig. 3.

B. Stillinger-Weber atomic interaction

The 2D atomic coordinates, say x and y, extracted from experimental images need to be completed by the z coordinates, corresponding to the hidden component perpendicular to the image plane. We introduce here a technique involving, in two steps, two energy-minimization calculations. These calculations are done with the widely used and successfully tested Stillinger-Weber potential [22] and with the parametrization of Ref. [23].

Far from the interface, the crystal structures of both grains are known and in particular the Si dumbbells correspond to atoms with two different altitudes z along the $[1\,\bar{1}\,0]$ direction, common to both grains. The crystal period along this direction is $s = a/\sqrt{2}$. We first assign a constant altitude $z = {}^{1}/_{2}\,s$ to all atoms except for the Si dumbbells far enough from the

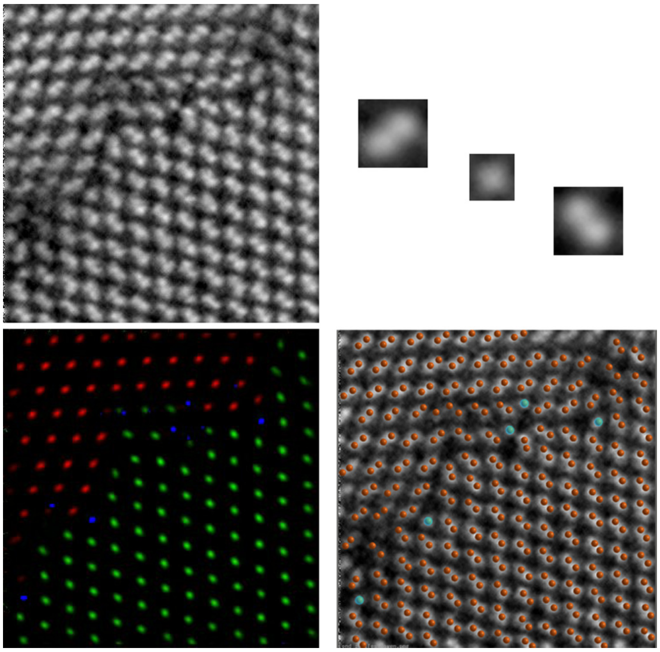

FIG. 3. Illustration of the pattern recognition technique. (Top left) Small part of an image, with grain II on top of grain I. (Top right) Three patterns corresponding to grains I, II, and to isolated atomic columns. (Bottom left) Color image representing the three correlation functions corresponding to the three patterns. Each correlation function represents one component of the RGB image coding (red, green, blue). A gamma correction of 4 has been applied to enhance the highest values of the correlations, i.e., a power-law function with exponent 4 is applied to the components (normalized between 0 and 1). (Bottom right) x and y atomic positions obtained by fitting, in the first image, individual or paired Gaussian functions, initially located at the maximum of the correlation functions. The individual atomic columns are distinguished by the color cyan.

interface to clearly belong to crystal sites. For these dumbbells, we set $z = {}^{1}/_{4}\,s$ and $z = {}^{3}/_{4}\,s$ to their respective two atoms. The isolated Si columns in Fig. 3 correspond to atoms linked by bonds parallel to $[1\,\bar{1}\,0]$ in order to be tetrahedrally bonded. This is incompatible with a single-period structure along this direction and instead the fourfold coordination symmetry implies a doubling of the period. To get the initial atomic configuration, the atomic layers of two periods are therefore stacked together along z, resulting in a periodicity of $2s$. Periodic boundary conditions are set along the z direction and free surface boundary conditions are set for x and y.

Doing a mere energy minimization starting from this configuration would be impossible because of the short interatomic distances resulting from the unrealistic identical z value settings. The configuration would be unpredictably destroyed during the minimization. In a first step, we instead minimize the energy taking the z coordinates as the only variables. Consequently, only the forces along z are involved and they are initially zero by symmetry except for the few atoms in the crystal grains that have been given different z values. At the beginning of the minimization, the surrounding of these few particularized atoms start to move, and then all the z coordinates are progressively revealed. When the z coordinates were first assigned, it made no difference which atom in a dumbbell is up and which atom is down as long as they are coherently displaced in the crystal. However, we have here two crystals and so we have a choice for the second grain once the first one is set. Considering the two possibilities, we have actually constructed two initial configurations that both have had their energy minimized with respect to the z coordinates. Despite these two possibilities, only one correct configuration is obtained. Depending on the cases, either both configurations converge to the same final configuration, or one can be easily discarded because of a residual antiphase boundary inside one of the grains.

As a second step, a regular energy minimization with respect to all coordinates is performed. This regularizes the crystalline structure of the grains since the experimental x and y data where extracted with some random fluctuations around the equilibrium atomic positions.

With the result obtained from an entire experimental image, two slices are cut from the final atomic configuration. The first one corresponds to a 7:5 approximant, the second one to a 10:7 approximant. For each structure, the slice width is chosen to be its ideal periodicity P introduced above [Eq. (2)]. Subsequent energy minimizations are performed to adjust the atomic positions to the new boundary conditions, but now with periodic boundary conditions for the x and z directions and free surface boundary conditions for y. As shown in Fig. 4, the final atomic configurations are in very good agreement with the corresponding parts of the experimental images. The coordinate files are available in Ref. [24]. Our numerical method has been able to resolve the pentagon and heptagon structures as well as the connectivity of the atoms corresponding to individual spots in the images. All the atoms are now tetra-coordinated.

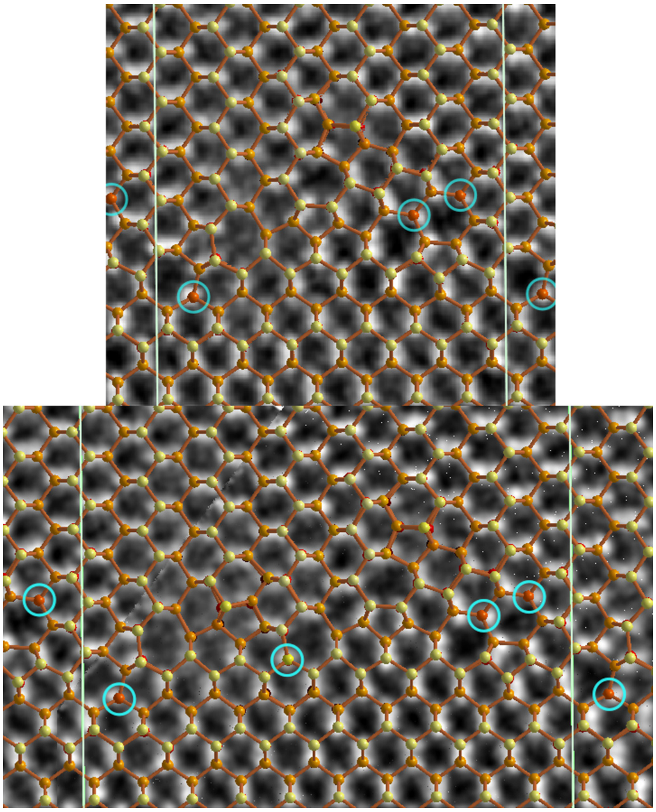

FIG. 4. Electron microscopy images overlaid by the atomic configurations of the 5:7 and 10:7 approximants stable with the Stillinger-Weber interactions (respectively top and bottom images). For the bottom image, two images has been combined to get a sharper contrast. The light vertical lines indicate the periodicity along the interface. The coordinates z perpendicular to the images are color coded from red (lower z) to yellow (higher z). All Si atoms are tetra-coordinated. Atoms connected by bonds orthogonal to the images are surrounded by cyan circles.

VI. FIRST-PRINCIPLE CALCULATIONS

BigDFT calculations

The approach presented in the previous section for recovering the atomic z coordinates can in principle be done with first-principal calculations in the density functional theory (DFT) framework. This is not possible in this study because of the large number of atoms to consider. However, the interface structure is far from the regular lattice structure of silicon. For instance, there are pentagonal and heptagonal Si loops instead of the usual hexagonal loops. Thus, to confirm the stability of the atomic configurations found with the effective interaction potential, we perform DFT calculations with the two approximants. This will also give us reliable interface energies. In this section, the configurations stable with Stillinger-Weber interactions are now the starting points for computing the electronic and atomic structures.

We have used BIGDFT code [17], which has the particularity of expressing the electronic wave functions with a set of wavelet basis functions. This characteristic makes it possible to control the computational precision in a systematic way, as with plane-wave basis functions, but furthermore gives a local decomposition of the wave functions. Besides the strong compression of the data and the excellent efficiency for parallel calculations both made possible by this locality, a variety of boundary conditions can be used, from isolated molecules to periodic crystals. This point is important here because we need to consider periodic conditions along x and z, but free boundary conditions along y. Indeed, the configurations are periodic approximant along x, the direction z of the interface is commensurate, and the y free boundary conditions correspond to a material slab with surfaces parallel to the interface. As usual, the perturbation by these external surfaces on the bulk electronic structure is minimized here by terminating the dangling bonds with hydrogen atoms. For the same purpose, no surface reconstruction is considered and the external Si atoms are set on their perfect lattice sites. Keeping these atoms fixed on both surfaces would be possible but would preclude any relative global shift of the grains, which is an important parameter of the grain-boundary structures. Instead, free-bloc conditions are used, i.e., all H atoms and the Si atoms in the two outermost external atomic layers at each surface are fixed all together, but their center of gravity follows the resultant of the forces applied to them. This feature has been implemented in the BIGDFT code [25] for this study.

To check the independence of the results on the slab width, two different sizes along the y direction are considered. In the 5:7 approximant, there are 48 H atoms and either 312

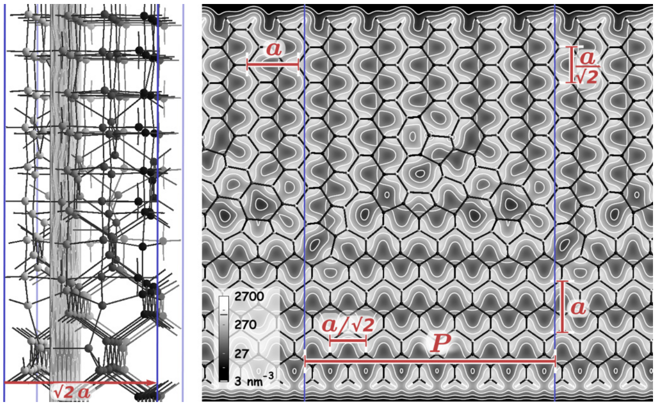

FIG. 5. Cross-section of the valence-electron density and ball-and-stick model of the 5:7 approximant. White and black in the gray-scale represent respectively the highest and the lowest electron density. (Left) Oblique view showing the location of the cross-section, which is perpendicular to the commensurate direction of the interface (common $[1\bar{1}0]$ direction). Along this direction, the periodicity of the structure is $\sqrt{2}\,a$, where a is the cubic lattice parameter of silicon. (Right) Plane view. The horizontal axis is the [001] direction of the upper grain and the [110] direction of the lower one. It is the opposite for the vertical axis. Along the incommensurate direction, P is the periodicity of the approximant. The logarithmic scale of the density plot is indicated by the gray-scale bar. The average density is $N_e/V = 196\ \text{nm}^{-3}$. The lattice parameter $a = 547$ pm gives the length scale. The free surfaces are passivated by hydrogen atoms.

or 408 Si atoms depending on the slab width. In the 10:7 approximant, there are 68 H atoms and either 440 or 576 Si atoms. Pseudopotentials [26,27] are used to simulate the core electrons. The Perdew-Burke-Ernzerhof (PBE) exchange correlation functional [28] is used in the calculation. The choice of the code, of the pseudopotentials, and of the PBE functional has been assessed in a general study [16] and gives high precision results. The k-point grid for calculations with the Si cubic cell is a $4 \times 4 \times 4$ Monkhorst Pack mesh. A $6 \times 4 \times 6$ mesh has been used for the orthogonal cell with paramerters $a/\sqrt{2}$, a and $a/\sqrt{2}$ (see Fig. 1). The real-space grid spacing between the wavelet-function centers, h_{grid}, is set to 21 pm corresponding to a high length resolution. With these conditions, the calculated value of the stable Si lattice parameter is 0.5466 nm in agreement with the nowadays DFT results [16]. For the grain-boundary calculations, the model periodicity along the z axis corresponds to two $[1\,\bar{1}\,0]$ periods and thus three k points are used in this direction. Because of the large value of the periodicity along x and the free-boundary conditions along y, no grid of k points is necessary for both of these axes.

The density functional calculations consist in minimizing the energy with respect to both the atomic positions and the electronic structure. The energy minimization is stopped when forces on the atoms are lower than 10 meV/Å. In the final configurations, all the Si atoms at the interface have kept their covalent bonding. The electronic density of the relaxed 7:5 approximant is shown in Fig. 5 and the coordinates of both approximants are available in Ref. [24].

The interface energy $\gamma_{\mathcal{I}}$ is estimated by removing the other energy contributions from the total potential energy E_{pot} of the configurations: Bulk energy ϵ_{Si}, the residual elastic energies due to the residual strains [Eq. (3)], and hydrogenated-surface energies $\gamma_{\text{H}\{1\,0\,0\}}$ and $\gamma_{\text{H}\{1\,1\,0\}}$. To calculate the surface energies, we also consider slab geometries for each of the two grain orientations (see Appendix and Fig. 11). Along y, the thickness of the slabs are similar to those of the grain-boundary configurations. Free surfaces are hydrogenated too. Complete density functional calculations are done for all slabs. Now by considering the same geometry for each grain, but with additional atomic layers to thicken the slabs, we can extract the bulk energy from their total energy differences. This way, we finally get three estimates of the bulk energy, one for each of the grain orientations plus one calculated merely from the cubic cell. The maximum discrepancy between them is only 2 meV per atom. This procedure is actually most useful to obtain all together bulk energy plus elastic energies of the slightly constrained grains. Indeed, the elastic constrains on the slabs are particular, with fixed strains along x and z (corresponding to imposed periodic conditions) and null stress along y (free-bloc conditions). Taking into account these auxiliary calculations, the computed interface energies $\gamma_{\mathcal{I}}$ are 0.652 and 0.667 J/m², respectively for the 7:5 and 10:7 approximants. The discrepancy between the thickest and thinnest slabs is less then 0.007 J/m². An estimate of $\gamma_{\mathcal{I}}$ for the infinite incommensurate grain boundary, and not approximants, will be given in Sec. VII and Table I.

TABLE I. Interfaces energies (J/m²) obtained in this work with DFT calculations and different parametrizations of the Stilling-Weber potential: $\gamma_{\mathcal{I},[7:5]}$, $\gamma_{\mathcal{I},[10:7]}$, and $\gamma_{\mathcal{I},[577:408]}$, respectively, for the periodic interfaces [7:5], [10:7], and [577:408]; $\gamma_{\mathcal{I}}$ for the incommensurate interface. Note that to compute these energies, the bulk terms have been removed, in particular the elastic energy of the periodic approximants. While $\gamma_{\mathcal{I},[7:5]} < \gamma_{\mathcal{I}} < \gamma_{\mathcal{I},[10:7]}$, the total energy is lower for the incommensurate interface, which has no long range elastic stress.

Atomic interactions	$\gamma_{\mathcal{I},[7:5]}$	$\gamma_{\mathcal{I},[10:7]}$	$\gamma_{\mathcal{I},[577:408]}$	$\gamma_{\mathcal{I}}$
DFT	0.652	0.667		0.660
S-W–Stillinger-Weber [22]	0.921	0.953	0.939	0.937
S-W–Vink *et al.* [23]	1.038	1.075	1.058	1.056
S-W–Pizzagalli *et al.* [41]	1.019	1.064	1.044	1.042

Another quantity, the adhesion energy γ_{A} is the gain per surface unit between the energy E_{pot} of the configuration and the energy it would have if the two grains would be separated. So here, the higher energy γ_{A}, the more stable is the interface. In our case, this last energy is deduced from slab calculations with a clean free surface on one side and hydrogenated surface on the other side. No complex surface reconstructions are taken into account, except the inter-plane relaxations, which are direct outputs of the calculation. The adhesion energy γ_{A} is equal to 3.26 J/m² for the 7:5 approximant. Though very close, the gain corresponds to a lower energy than the reported value $\gamma_{\text{A}} = 3.2$ J/m² for an alternate structure of the 7:5 approximant [9]. For the 10:7 approximant, γ_{A} is found equal to 3.21 J/m². The energy γ_{A} for separating the grains can be compared to the energies 4.65 and 3.38 J/m² obtained in this work for cleaving Si crystal at (1 0 0) and (1 1 0) surfaces, respectively. These values are similar to those found in Ref. [9].

VII. FROM APPROXIMANTS TO A COMPLETE DESCRIPTION OF THE INTERFACE

A. Hyperspace description and substitution rules

The Fibonacci tiling, or Fibonacci word, is a prototype of 1D quasicrystals [29]. It is regularly presented to illustrate the strip and projection method [30,31], the cut method [32,33] or the inflation-rule method [12,29,34]. These methods generate or describe the quasicrystalline structures. The Fibonacci tiling is closely related to the golden ratio, i.e., the irrational number $\varphi = (1+\sqrt{5})/2$. Here, to combine together replicas of the two approximants described in the previous sections and get an incommensurate grain boundary, we derive similar properties for a tiling now based on $\sqrt{2}$ and associated with the silver ratio $\delta_S = 1+\sqrt{2}$ instead of the golden ratio φ. To comply with the usual notations and broaden the scope of the discussion, we denote $\mathbf{S} = [7:5]$ and $\mathbf{L} = [10:7]$ the two approximants now regarded as structural units, with respective numbers N_S and N_L in a given sequence (**S** for small and **L** for large).

First of all, why a grain boundary should be associated with such a tiling related to $\sqrt{2}$? The answer is given by Eqs. (3). They show that the sequence of structural units should maintain, locally and globally, the ratio n_s/n_ℓ the closest as possible to $\sqrt{2}$ in order to minimize the strain and thus the stress in the grains. It can be easily tested that for a sequence of N_S and N_L units with $N_\mathrm{S}+N_\mathrm{L} \to \infty$, the limit of $n_s/n_\ell = (7N_\mathrm{S}+10N_\mathrm{L})/(5N_\mathrm{S}+7N_\mathrm{L})$ is $\sqrt{2}$ when the limit of $N_\mathrm{S}/N_\mathrm{L}$ is itself $\sqrt{2}$. The lengths P_L and P_S of the two units are identified with their periods along x [see Eqs. (2)] and the ratio $P_\mathrm{L}/P_\mathrm{S}$ is equal to $\sqrt{2}$.

The strip and projection method is a method of choice to generate an incommensurate tiling (or sequence) of **S** and **L** units. To get a $\sqrt{2}$ tiling, a strip of slope $\sqrt{2}$ is used to select points of coordinates $(N_\mathrm{L}, N_\mathrm{S})$ from a 2D simple square lattice. This is illustrated in Fig. 6 with the strip derived from the elementary lattice cell. This correspond to a very simple algorithm using the deviation Δ introduced in Eq. (1). Starting from no units, we add them one by one with the following rule: From N_S and N_L units, add one new **S** unit if $\Delta[N_\mathrm{S}+1, N_\mathrm{L}] < 1$, if not add a **L** unit. In the last case, the numbers satisfied the relation $\Delta[N_\mathrm{S}, N_\mathrm{L}+1] \leqslant \sqrt{2}$. These two inequalities are linked to the strong condition for the best rational approximation seen in Sec. III. Figure 7 shows the relation between the strip-method and the residual strain due to the lattice misfit at the interface.

In these $\sqrt{2}$ tilings, the units can be grouped into larger tiles $\mathbf{L_1}$ and $\mathbf{S_1}$, which have a length ratio of $\sqrt{2}$ too. This gives the substitution rules:

$$\mathbf{L} \to \mathbf{L}_1 \equiv \mathbf{SLS}, \tag{4a}$$

$$\mathbf{S} \to \mathbf{S}_1 \equiv \mathbf{LS}, \tag{4b}$$

where, in the context of this paper, $\mathbf{L}_1$ and $\mathbf{S}_1$ are periodic grain boundaries corresponding to juxtapositions of elementary periods of the grain boundaries $\mathbf{L} \equiv \mathbf{L}_0$ and $\mathbf{S} \equiv \mathbf{S}_0$. Grain boundary $\mathbf{S}_1$ corresponds to the convergent structure [17 : 12] and $\mathbf{L}_1$ to the semi-convergent structure [24 : 17]. Starting from an initial unit and iterating the substitution rules (4) generates periodic tilings of increasing period. Equivalent by construction, an alternative method consists of using the recurrence relations

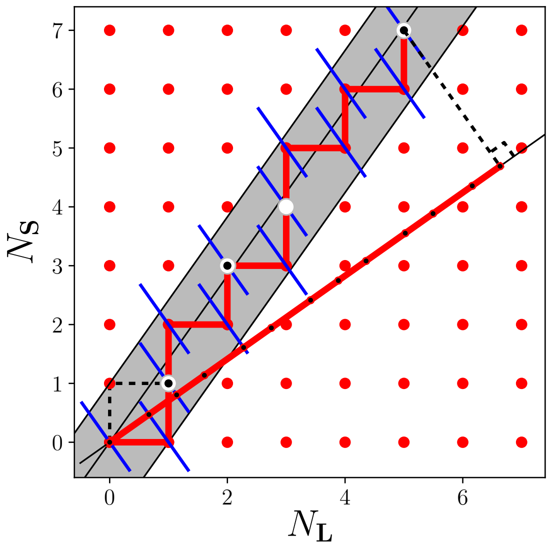

FIG. 6. Strip and projection method to generate a $\sqrt{2}$ tiling from the square lattice. The gray strip has a slope equal to $\sqrt{2}$ fixing the ratio $N_\mathrm{S}/N_\mathrm{L} = \sqrt{2}$. The lower limit of the strip goes through the point (1, 0) and the upper limit through (0,1). The strip is half-bounded with the upper limit excluded here. The square edges and the sites of the square lattice inside the strip are selected. Once projected onto a straight line, they correspond respectively to the tiles and vertices of the tiling. If projected onto a line of slope $\sqrt{2}$ identical to the slope of the strip, the length of the segments would be in the ratio $P_\mathrm{L}/P_\mathrm{S} = 1/\sqrt{2}$. To get the ratio $P_\mathrm{L}/P_\mathrm{S} = \sqrt{2}$, they are projected onto a line of slope $1/\sqrt{2}$. The equivalence with the cut method is also sketched: A line segment is periodically set on every site of the lattice (for clarity only those selected by the strip are drawn). The vertices of the tiling are now the intersection points between all segments and the line of slope $\sqrt{2}$ going through the origin. To get the correct length ratio, the segments are perpendicular to the line with slope $1/\sqrt{2}$. The common length of the segments is the width of the strip along this direction. The white disks inside the strip correspond to the best rational approximations $N_\mathrm{S}/N_\mathrm{L}$ of $\sqrt{2}$, i.e., $|N_\mathrm{S}/N_\mathrm{L} - \sqrt{2}| < |p/q - \sqrt{2}|, \forall\, q \leqslant N_\mathrm{L}$. Among them, those with a central black dot correspond to the continued-fraction convergents, which are solutions of the stronger condition Eq. (1).

$$\mathbf{L}_n = \mathbf{S}_{n-1}\mathbf{L}_{n-1}\mathbf{S}_{n-1}, \tag{5a}$$

$$\mathbf{S}_n = \mathbf{L}_{n-1}\mathbf{S}_{n-1}, \tag{5b}$$

and generating two sets of sequences in parallel. Since at step zero the ratio $P_\mathrm{L}/P_\mathrm{S}$ of the tile lengths is $\sqrt{2}$, these relations show that the length ratio of $\mathbf{L}_n$ and $\mathbf{S}_n$ is still $\sqrt{2}$ for any generation n, and that these lengths increase by a factor $\delta_S = 1+\sqrt{2}$ after each substitution. The original substitution rules leading to the Fibonacci tiling are $\mathbf{L} \to \mathbf{LS}$ and $\mathbf{S} \to \mathbf{L}$, with the transformation of the numbers N_S and N_L from one generation to the other strongly linked to the golden ratio φ. For the $\sqrt{2}$ tiling, the matrix **M** that relates the column vector $(N_\mathrm{L}; N_\mathrm{S})$ before and after one substitution is

$$M = \begin{pmatrix} 1 & 1 \\ 2 & 1 \end{pmatrix}. \tag{6}$$

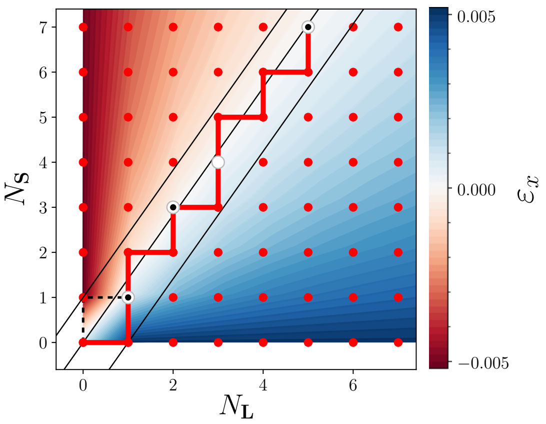

FIG. 7. Density plot of the strain $\varepsilon_{x,\mathrm{II}}$ in grain II for sequences made of N_L tiles **L** and N_S tiles **S** due to the misfit between the periodicities along the incommensurate direction of the two crystalline grains [see Eqs. (3)]. Strain $\varepsilon_{x,I}$ in grain I is the opposite. The red line (bold polygonal curve) represents $\mathbf{S}_3 = \mathbf{LSSLSLSSLSLS}$ [Eqs. (4)], a sequence that minimizes the strain field locally and on average.

The two eigenvalues of **M** are the silver ratio $\delta_S = 1 + \sqrt{2}$ and its conjugate $1 - \sqrt{2} = -1/\delta_S$. Since they are the solutions of a quadratic equation, i.e., the characteristic equation $(1 - x)^2 - 2 = 0$, with a module greater than unity for the first one and smaller than unity for the second one, the eigenvalue δ_S is a Pisot number. This property is coherent with the fact that we are constructing a quasicrystalline tiling [34–36]. The vector $(1, \sqrt{2})$ is an eigenvector of **M** corresponding to the largest eigenvalue δ_S. Therefore the ratio $N_\mathrm{S}/N_\mathrm{L}$ and thus the ratio n_s/n_ℓ tend to $\sqrt{2}$ when the number of successive substitutions tends to ∞. Thus, in both grains and away from the interface, the residual strain due to the lattice parameter mismatch actually tends to zero [see Eq. (3)].

Note 1. The $\sqrt{2}$-sequence described in this work is very closely related to the octonacci sequence [37–40]:

$$\mathbf{L}' \rightarrow \mathbf{S}'\mathbf{L}'\mathbf{L}' \quad \text{and} \quad \mathbf{S}' \rightarrow \mathbf{L}' \tag{7}$$

(different orders in the tile concatenations in Refs. [37,39,40]). Indeed, both sequences have the recurrence relation

$$\mathbf{S}_n = \mathbf{S}_{n-2}\mathbf{S}_{n-1}\mathbf{S}_{n-1} \tag{8}$$

deduced here from Eqs. (5a) and (5b). One sequence is related to the other by choosing $\mathbf{L}' = \mathbf{LS}$ and $\mathbf{S}' = \mathbf{S}$. So, getting one or the other is a matter of the choice of the two basic tiles, **L** in the $\sqrt{2}$ sequence being smaller than $\mathbf{L}'$. Since the elementary blocks **L** and **S** are directly extracted from the electron micrographs, the $\sqrt{2}$ sequence appears as a natural choice here.

Note 2. For simplicity in the Fibonacci tiling, the length ratio of the **L** and **S** tiles are usually set to φ, i.e. the same value as the tile proportion $N_\mathrm{L}/N_\mathrm{S}$. That way, in the strip-and-projection method on a square 2D-lattice, the strip selects the tiles and a projection orthogonal to it gives directly the tiles. Here, in the $\sqrt{2}$ tiling, the length ratio is fixed to $\sqrt{2}$ by the periodicity of the approximants $\mathbf{L} = [10 : 7]$ and $\mathbf{S} = [7 : 5]$ observed by microscopy, while their proportion $N_\mathrm{L}/N_\mathrm{S}$ is the inverse $1/\sqrt{2}$ to minimize the strain in the Si crystals. Thus the strip and the direction of the projection are not orthogonal as shown in Fig. 6. Equivalently in the cut method, the segment motif of the 2D-unit cell is not orthogonal to the strip direction, as shown in Fig. 6 too. A similar result could be obtained from a rhombic 2D lattice.

Note 3. While the infinite quasicrystalline $\sqrt{2}$ tiling corresponds to the slope $\sqrt{2}$, finite sequences $\mathbf{L}_n$ or $\mathbf{S}_n$ can be obtained from the square 2D lattice with slopes $N_\mathrm{S}/N_\mathrm{L}$. That way, the strip-and-projection method leads to periodic 1D lattices with $\mathbf{L}_n$ or $\mathbf{S}_n$ as the unit cells. Since in our case, the tiles **L** and **S** are periodic approximants at the atomic scale, we can build atomistic structures with periodic boundary conditions along the interface. These structures are thus well suitable for simulations at the atomic level.

Note 4. From Fig. 7, we can deduce that a random sequence of **L** and **S** units would increase the material strain and thus its elastic energy. This would also be the case, for instance, for sequences generated by the rules $\mathbf{L} \rightarrow \mathbf{LSLSL}$ and $\mathbf{S} \rightarrow \mathbf{SLSS}$ whose substitution matrix has the same eigenvectors than matrix **M** Eq. (6) leading to the same tile ratio $N_\mathrm{S}/N_\mathrm{L} = \sqrt{2}$. However its largest eigenvalue, $3 + \sqrt{2}$, is not a Pisot number; the smallest, $3 - \sqrt{2}$, is larger than unity. As a consequence [34–36], the extension perpendicular to the strip diverges in the square lattice of Fig. 7 and would thus correspond to a material with a larger strain.

B. Application of the substitution rules

With the recurrence rules and the atomistic configurations of the structural units, large models of the grain boundary can now be generated. Figure 8 shows part of a 41:29-approximant overlaying the experimental image of figure 2 in a very satisfactory way (sequence **LSSLS** equivalent to $\mathbf{S}_2$ by periodicity). These larger models can be easily relaxed with the Stillinger-Weber potential [23], which we started with in Sec. V. The agreement is satisfactory too and Fig. 8 shows a correlation between the highest atomic energies and the fuzziness of the experimental spots.

The interface energy $\gamma_\mathcal{I}$ of the incommensurate grain boundary can now be estimated too (see Appendix). Indeed, neglecting the correlation effects between structural units, the interface energies per 2D unit cell of the 7:5 and 10:7 approximants (Sec. VI) can be weighted by their respective concentrations, $\sqrt{2}/\delta_S$ and $1/\delta_S$. The 2D-unit cell areas $\sqrt{2}\,a\,P_{7:5}$ and $\sqrt{2}\,a\,P_{10:7}$ are averaged with the same respective weights (the z periodicity, $\sqrt{2}\,a$, corresponds to two $[1\,\bar{1}\,0]$ periods because of the interface reconstruction; the x periodicity corresponds to P in equation 2). Dividing the weighted energy average by the weighted area average yields to $\gamma_\mathcal{I} = 0.660$ J/m². Calculated in the same way, the calculated adhesion energy of the incommensurate grain boundary is $\gamma_\mathrm{A} = 3.23$ J/m².

For reference, we also have computed the interface energy $\gamma_\mathcal{I}$ obtained with the Stillinger-Weber potential [23]. This value, as well as the value obtained with the original parametrization by Stillinger and Weber [22] are given in Table I. A recent potential parametrization [41] has also been tested and the result is included in table I. Since much larger configurations can be considered using Stillinger-Weber interactions than by DFT calculations, the interface energy of the 577:408 approximant has also been calculated for these

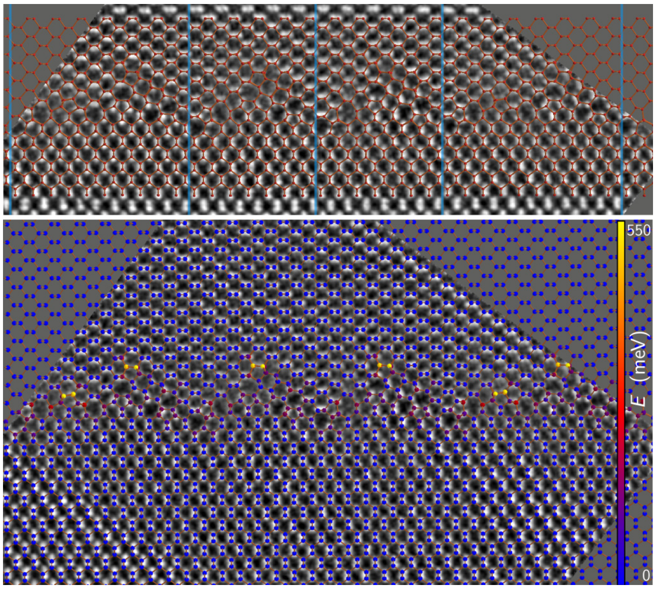

FIG. 8. (Top) Overlay of the experimental image by a sequence of **S** and **L** tiles, i.e., respectively, the [7 : 5] and [10 : 7] approximants, each one calculated by DFT. The vertical lines indicate the tile boundaries. (Bottom) Overlay of the experimental image by a [41 : 29] approximant corresponding to the sequence $\mathbf{S}_2$, now relaxed with the Stillinger-Weber potential [23]. The energy of the atoms with this potential is color coded (online version) from blue (bulk energy) to red and yellow (highest energy). Note that the image contrast is correlated with the atom energies: When a high energy has been found the contrast is lower, probably indicating structure perturbations like a higher vacancy concentration or larger atomic moves.

interatomic potentials. This approximant corresponds to the sequence S_5 made of 41 S and 29 L units. It has a period P equal to 221.6 nm along the incommensurate direction. This gives the opportunity to check the validity of partitioning the whole grain boundary into S and L units to compute the interface energy, while neglecting the correlation effects. Indeed, the relative difference is only 0.2% between $\gamma_{\mathcal{I}}$ and $\gamma_{\mathcal{I},[577:408]}$ taking into account long range elastic stresses as discussed in Ref. [15] (see Table I). With the large 577:408 approximant and the Stillinger-Weber potential [23], we can also test the energy difference resulting from alternative sequences of S and L units. We have tested a random sequence of 41 S and 29 L and the extreme case where the S and L units are segregated. In both cases, the energy minimizations lead to a deformation of the layer due to the strain. The interface is not flat anymore and the buckling is larger for the segregated sequence than for the random one. To avoid this artifact, the minimization has been redone with constrains. The y and z coordinates of the first layer at each surface have been fixed, while the x coordinates were unconstrained to let the strain field adjust to the S and L stacks along x. The incommensurate sequence has the lowest energy, while the random and the segregated ones have a surplus of 1 and 7 mJ/m², respectively. These results are coherent with the strain analysis illustrated in Fig. 7. The random and the segregated sequences have excursions far from the ideal S and L concentrations, the segregated one being the extreme case.

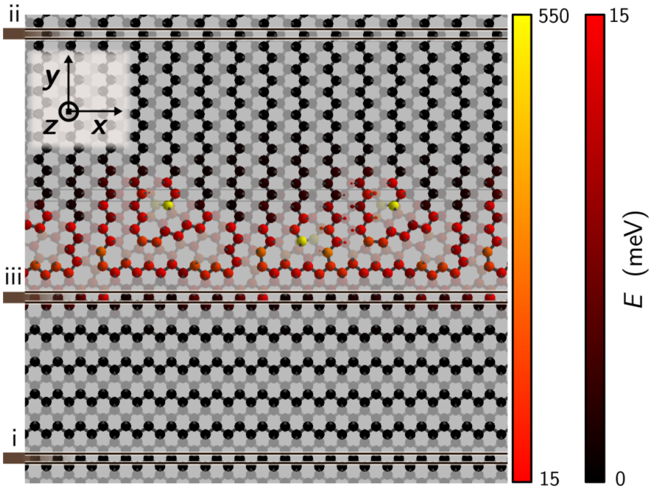

FIG. 9. Atomic-configuration visualization highlighting the calculation of the hull functions Δx and Δy plotted in Fig. 10. Only one atomic layer perpendicular to z is not shaded by a transparent mask. Far from the interface, the atoms selected by the two lowest horizontal lines are representative of a crystalline atomic row, *i*, of grain I. In the same way, the two highest horizontal lines correspond to an atomic row, *ii*, of grain II. At the interface, the horizontal lines correspond to an atomic row, *iii*, that has been chosen for calculating its hull plots. Any atomic row could be selected, however this one is the closest to the interface with atoms having the same first-neighbor environment than those of grain I. That way, the influence of grain II on grain I can be analyzed. The opposite would be possible by choosing an atomic row in grain II. To simplify the discussion, row *i* has been chosen to select crystallographically equivalent lattice sites than those of row *iii*. The atomic configuration has been relaxed with the Stillinger-Weber potential [23] to get atomic energies. These energies are color coded with two successive color gradients. From zero to 15 meV, the first scale shows the energy range in rows *iii*. From 15 to 550 meV, the second scale highlights the high energy spots at the interface.

C. Hull plots

Sharing the same cubic misorientation than the present Si grain boundary, the 90° ⟨1 1 0⟩ tilt grain boundary in gold is therefore also an incommensurate grain boundary. For gold, it has been shown that this grain boundary has a frictionless—or superglide—property [20,43,44]. Such a property was first introduced for a unidimensional theoretical model of atoms in a periodic potential field [45,46]. Then, it was theoretically studied and experimentally found in several studies on friction [42,43,47–61].

The frictionless property is unlikely for this silicon interface, because of its reconstruction extension with faceting clearly visible on the calculated-structure image (Fig. 9) as well as on the experimental images (Fig. 2 and in Refs. [5,6,19]). However, Aubry hull-function analysis [45,62] is the way to get a clear signature of this dynamical property from the static structure of an incommensurate atomic configuration. The hull function characterizes the atomic relaxation from a periodic lattice when the atoms are subject to a periodic potential having a different and incommensurate periodicity. Depending on the strength of the interactions, two regimes exist separated by an Aubry transition

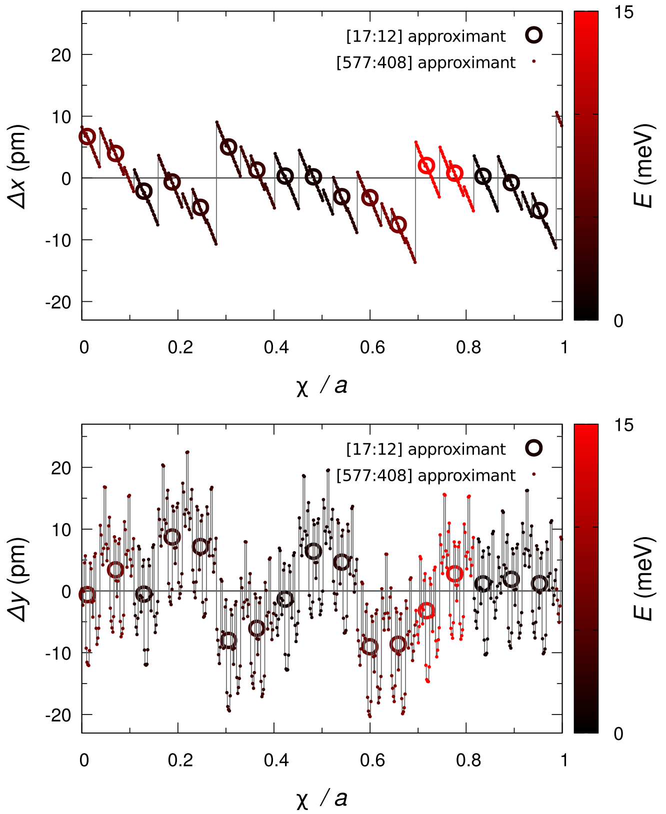

FIG. 10. Hull plots of the first atomic row of grain I at the incommensurate interface (see row iii of the lower grain in Fig. 9). The lattice parameter a is also the periodicity ℓ of grain II. (Top) Atomic relaxation Δx along the incommensurate direction. (Bottom) Relaxation Δy perpendicular to the interface. The Δy origin corresponds to the average of the y coordinates in row *iii*. These hull plots are calculated with 17 Si atoms of the [17:12] approximant (large circles) and 577 atoms of the [577:408] approximant (small dots). Function discontinuities cannot be revealed by inspecting the [17:12] results. However, note that the atomic relaxations of the [17:12] approximant are representative of those of the [577:408] one, the small-model data following the trends of the large-model ones. The discontinuities and the apparent fuzziness of the [577:408] curves are intrinsic to this type of incommensurate interface. The curves could be continuous for another material, but here they are discontinuous everywhere. It is a pinned-state characteristic [42].

corresponding to a "breaking of analyticity" [45] when going from the unpinned states to the pinned one. Since the original unidimensional Frenkel-Kontorova case, the hull function has been generalized to more complex systems [20,51,63].

At a grain boundary, each crystal row parallel to the incommensurate direction is perturbed by the other crystal and we consider the displacements of the atoms from their ideal lattices positions. Thus we need these lattices positions, and a reference can be selected far from the interface. This is illustrated in Fig. 9 where rows *i* and *ii* are representative of the lattice grains I and II, respectively.

To represent the hull modulation function Δx (see Fig. 10), the atomic displacements are plotted versus the place of their ideal sites relative to the perturbation, i.e., the other lattice periodicity. In grain I with period s along x, the ideal coordinate of an atom with a lattice index $j \in \mathbb{Z}$, is $x_{0\,j} = j\,s + \alpha$. The shift α is the x coordinate of one arbitrary atom of row *i*, the origin being set here on one arbitrary atom of row *ii*. The relaxation displacement of an atom in row *iii*, i.e., its modulation from the ideal lattice site, is $\Delta x_j = x_j - x_{0\,j}$. This displacement Δx_j is plotted versus $\chi_j = (x_{0\,j} \text{ modulo } \ell)$, where ℓ is the periodicity of grain II. The system being invariant by a shift ℓ of grain I because of the grain II periodicity, the modulo function wraps the complete relaxation behavior of the atoms in a function defined on $[0, \ell[$. The relaxation Δy_j perpendicular to the interface versus χ_j is also plotted in Fig. 10. Here, $\Delta y_j = y_j - \bar{y}$, where $\bar{y}$ is the average of the y_j in row *iii*. Using a lattice reference rather than $\bar{y}$ for calculating Δy_j is also possible and would only result in a shift of the origin for Δy_j.

The discontinuous nature of the hull functions is clearly visible in Fig. 10. An infinitesimal glide of grain I relative to grain II, would correspond to an infinitesimal change of the coordinates $x_{0\,j}$ and consequently to the quantity χ_j ($\in [0, \ell[$). Discontinuities of $\Delta x(\chi)$ would lead to finite jumps of the atomic displacements, and thus the system would have to overcome energy barriers. Therefore this Si grain boundary has a pinned behavior and not a superglide one. The "broken analyticity" is particularly visible in the Δy hull plot.

VIII. CONCLUSION

A general description of an incommensurate grain boundary in silicon has been given. While this paper is focused on a precise structure, it illustrates a general methodology for semiconductors different from the analysis of incommensurate boundaries in metals [20,42,43]. This differences are mainly related to the behavior of the atomic bindings. Because of the covalent bonds, the boundary here is a quasicrystalline sequence of two elementary units with opposite internal strains: The 7:5 approximant **S** and the 10:7 approximant **L**. First, these units have been selected since they are present in the experimental electron-microscopy images. Second, the unit **S** corresponds to the ratio 7/5, one of the first best rational approximants of $\sqrt{2}$, while the unit **L** is a kind of complementary unit to **S** because of its almost opposite residual strain. Unit **L** corresponds to the semiconvergent ratio 10/7 of $\sqrt{2}$. So, in the material, these two units can be combined together in a suitable way to reduce the strain and stress resulting from the incommensurate periodicities of the crystals on both sides of the boundary. For instance, concatenating **L** with **S** gives **LS**, which corresponds to the next best rational approximant 17/12.

For both elementary units, we have conducted a detailed analysis of the 2D images obtained by electron microscopy. A pattern recognition technique has been applied on high resolution images and has given reliable in-plane coordinates of the atomic spots. Taking advantage of the three components of color coding, the three correlation functions of the characteristic patterns—two orthogonal dumbbells and one single spot—can be combined together to give a comprehensive image of the grain-boundary. The three-dimensional atomic coordinates have been resolved with atomic-forces calculations using a Stilling-Weber potential and a two-step method. A first energy minimization is conducted, restricted only to the

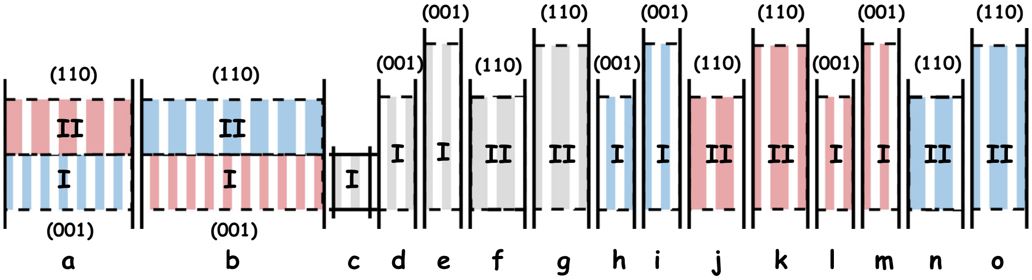

FIG. 11. Schematic view of the configurations constructed with grains I and II to compute the interface energy $\gamma_{\mathcal{I}}$. The solid lines represent the periodic boundary conditions. The dashed lines show the interfaces and the free surfaces of types (001) or (110). Configurations a and b are the 7:5 and 10:7 approximants, respectively. The tensile and compressive residual strains are shown in blue and red colors, respectively. These strains are due to the incommensurability between grain I and grain II periodicities. For taking into account their effects on the elastic energy and on the surface energies, these strains have been applied to configurations h to o. More precisely, the strains present in the 7:5 approximant (configuration a) have been used in configurations h to k, while those of the 10:7 approximant (configuration b) have been used in l to o. The different layer widths, for instance, between configurations n and o, allow us to separately determine the strained-bulk energy and the strained-surface energy. Indeed, only the numbers of bulk atoms are different, while the free-surface areas are identical. Configuration c is a simple crystalline cell used to compute the reference bulk energy. Without applied strain too, configurations d to g provide us with two other ways to compute the bulk energy, as well as the values of the surface energies $\gamma_{\{0\,0\,1\}}$ and $\gamma_{\{1\,1\,0\}}$.

atomic coordinates perpendicular to the plane view. Once the third coordinates are recovered, the second step is an usual minimization that rectifies coherently all the coordinates of the structure. Finally, the structure has been refined with electronic structure calculations. The resulting **S** and **L** structures are fourfold-coordinated silicon networks and are perfectly periodic in the two dimensions of the boundary.

To give a complete atomic description of the incommensurate boundary, the elementary units should form a sequence that reduces the interface stress. With tools adapted for quasicrystals, the atomic structures of **S** and **L** units can be combined together. In particular, we have given inflation rules related to the silver ratio and suitable for **S** and **L** tilings. Si atoms are still fourfold-coordinated in the resulting interfaces.

Suitable for incommensurate structures, the hull function of the grain boundary has been calculated, thanks to the large systems that can be constructed with the inflation rules. It demonstrates that no hypofriction property can be expected here.

This paper describes a structure corresponding to a perfect incommensurate interface minimizing the residual stress in the grains. However, defects of this ideal structure should be present in real materials, depending on the elaboration process. This is indeed what has been observed by electron microscopy and a rich variety of situations can be imagined. It is however out of the scope of this paper to describe them here.

ACKNOWLEDGMENT

The authors thank A. Marty for useful discussions and suggestions.

APPENDIX: INTERFACE-ENERGY CALCULATION

To extract the interface energy $\gamma_{\mathcal{I}}$ of a grain boundary from the total energy E_{total} of a configuration made of two crystalline grains, one must separately compute the bulk energy ϵ_{atom} and the free surfaces ones γ_{surfaces} to remove their contributions from E_{total}:

$$\gamma_{\mathcal{I}}\, S_{\mathcal{I}} = E_{\text{total}} - N_{\text{total}}\, \epsilon_{\text{atom}} - \gamma_{\text{surfaces}}\, S_{\mathcal{I}},$$

where $S_{\mathcal{I}}$ is the area of the grain boundary and N_{total} is the number of atoms in the configuration. In this paper, we determine $\gamma_{\mathcal{I}}$ of an incommensurate grain boundary from the contributions of its periodic grain-boundary units. These units are slightly constrained due to the incommensurate periodicities of the grains, while the incommensurate grain boundary itself has no intrinsic long range strain. Thus, to carefully calculate $\gamma_{\mathcal{I}}$, we must generalize the previous equation. The configurations taken into account are shown schematically in Fig. 11. For instance, from the total energy E_{total} of the 7:5 configuration ("a" in Fig. 11), we calculate

$$\begin{aligned}\gamma_{\mathcal{I},[7:5]}\, S_{\mathcal{I},[7:5]} = {} & E_{\text{total}} - N_{\text{I}}\, \epsilon_{\text{h,i}} - N_{\text{II}}\, \epsilon_{\text{j,k}} \\ & - \gamma_{\text{h,i}}\, S_{\mathcal{I},[7:5]} - \gamma_{\text{j,k}}\, S_{\mathcal{I},[7:5]},\end{aligned}$$

where $\epsilon_{\text{h,i}}$ and $\gamma_{\text{h,i}}$ are the strained bulk and surface energies calculated from configurations "h" and "i" in Fig. 11. Similarly, $\epsilon_{\text{j,k}}$ and $\gamma_{\text{j,k}}$ are derived from configurations "j" and "k." Area $S_{\mathcal{I},[7:5]}$ is the interface area of the 7:5 unit. In the same way, $\gamma_{\mathcal{I},[10:7]}$ can be calculated with the energies of configurations "b" and "l" to "o."

Finally, taking into account the respective frequencies $c_{\text{S}} = \sqrt{2}/\delta_S$ and $c_{\text{L}} = 1/\delta_S$ of units $\mathbf{S} = 7:5$ and $\mathbf{L} = 10:7$, the interface energy of the incommensurate grain boundary is

$$\gamma_{\mathcal{I}} = \frac{c_S\, \gamma_{\mathcal{I},[7:5]}\, S_{\mathcal{I},[7:5]} + c_L\, \gamma_{\mathcal{I},[10:7]}\, S_{\mathcal{I},[10:7]}}{c_S\, S_{\mathcal{I},[7:5]} + c_L\, S_{\mathcal{I},[10:7]}}.$$

[1] F. Fournel, H. Moriceau, B. Aspar, K. Rousseau, J. Eymery, J.-L. Rouvière, and N. Magnea, Accurate control of the misorientation angles in direct wafer bonding, Appl. Phys. Lett. **80**, 793 (2002).

[2] A. Sakai, Characterization of wafer-bonded substrates for advanced channels in Si-based MOSFET, in *Proceedings of 2010 10th IEEE International Conference on Solid-State and Integrated Circuit Technology, 2010* (IEEE, Piscataway, NJ, 2010), pp. 1517–1520.

[3] E. Toyoda, A. Sakai, O. Nakatsuka, H. Isogai, T. Senda, K. Izunome, M. Ogawa, and S. Zaima, Characterization of bonding structures of directly bonded hybrid crystal orientation substrates, Thin Solid Films **517**, 323 (2008).

[4] E. Toyoda, A. Sakai, H. Isogai, T. Senda, K. Izunome, K. Omote, O. Nakatsuka, and S. Zaima, Characterization and analyses of interface structures in directly bonded Si(011)/Si(001) substrates, Jpn. J. Appl. Phys. **48**, 021208 (2009).

[5] J.-L. Rouvière, F. Lançon, K. Rousseau, D. Caliste, P.-H. Jouneau, and F. Fournel, Structure of an incommensurate 90° Si grain boundary resolved with the help of a Cs-corrector for illumination, J. Phys.: Conf. Ser. **209**, 012041 (2010).

[6] T. Signamarcheix, B. Biasse, A.-M. Papon, E. Nolot, F. Mazen, J. Leveneur, O. Faynot, L. Clavelier, and B. Ghyselen, Crystallographic orientation engineering in silicon-on-insulator substrates, Appl. Phys. Lett. **96**, 262111 (2010).

[7] T. Kato, Y. Nakamura, J. Kikkawa, A. Sakai, E. Toyoda, K. Izunome, O. Nakatsuka, S. Zaima, Y. Imai, S. Kimura, and O. Sakata, Structural change of direct silicon bonding substrates by interfacial oxide out-diffusion annealing, Thin Solid Films **518**, S147 (2010).

[8] C.-Y. Sung, H. Yin, H. Y. Ng, K. L. Saenger, V. Chan, S. W. Crowder, J. Li, J. A. Ott, R. Bendernagel, J. J. Kempisty, V. Ku, H. K. Lee, Z. Luo, A. Madan, R. T. Mo, P. Y. Nguyen, G. Pfeiffer, M. Raccioppo, N. Rovedo, D. Sadana *et al.*, High performance cmos bulk technology using direct silicon bond (dsb) mixed crystal orientation substrates, in *IEEE International Electron Devices Meeting, 2005, IEDM Technical Digest* (IEEE, Piscataway, NJ, 2005), pp. 225–228.

[9] H. Kariyazaki, T. Aoki, K. Izunome, and K. Sueoka, Molecular simulation on interfacial structure and gettering efficiency of direct silicon bonded (110)/(100) substrates, J. Appl. Phys. **107**, 113509 (2010).

[10] N. Rivier, A botanical quasicrystal, J. Phys. Colloques **47**, C3-299 (1986).

[11] D. Gratias and A. Thalal, Hidden symmetries in general grain boundaries, Philos. Mag. Lett. **57**, 63 (1988).

[12] A. P. Sutton, Irrational tilt grain boundaries as one-dimensional quasicrystals, Acta metall. **36**, 1291 (1988).

[13] P. A. Deymier, M. Shamsuzzoha, and J. D. Weinberg, Experimental evidence for a structural unit model of quasiperiodic grain boundaries in aluminium, J. Mater. Res. **6**, 1461 (1991).

[14] A. P. Sutton, Irrational interfaces, Prog. Mater. Sci. **36**, 167 (1992).

[15] A. P. Sutton and R. W. Balluffi, *Interfaces in Crystalline Materials* (Oxford University Press, New York, 1995).

[16] K. Lejaeghere, G. Bihlmayer, T. Björkman, P. Blaha, S. Blügel, V. Blum, D. Caliste, I. E. Castelli, S. J. Clark, A. Dal Corso, S. de Gironcoli, T. Deutsch, J. K. Dewhurst, I. Di Marco, C. Draxl, M. Dulak, O. Eriksson, J. A. Flores-Livas, K. F. Garrity, L. Genovese *et al.*, Reproducibility in density functional theory calculations of solids, Science **351**, aad3000 (2016).

[17] L. Genovese, A. Neelov, S. Goedecker, T. Deutsch, S. A. Ghasemi, A. Willand, D. Caliste, O. Zilberberg, M. Rayson, A. Bergman, and R. Schneider, Daubechies wavelets as a basis set for density functional pseudopotential calculations, J. Chem. Phys. **129**, 014109 (2008).

[18] F. Lançon, L. Genovese, and J. Eymery, Towards simulation at picometer-scale resolution: Revisiting inversion domain boundaries in GaN, Phys. Rev. B **98**, 165306 (2018).

[19] N. Cherkashin, O. Kononchuk, S. Reboh, and M. Hÿtch, Application of the O-lattice theory for the reconstruction of the high-angle near 90° tilt Si(110)/(001) boundary created by wafer bonding, Acta Mater. **60**, 1161 (2012).

[20] A. Gautam, C. Ophus, F. Lançon, V. Radmilovic, and U. Dahmen, Atomic structure characterization of an incommensurate grain boundary, Acta Mater. **61**, 5078 (2013).

[21] S. Paciornik, R. Kilaas, J. Turner, and U. Dahmen, A pattern recognition technique for the analysis of grain boundary structure by HREM, Ultramicroscopy **62**, 15 (1996).

[22] F. H. Stillinger and T. A. Weber, Computer simulation of local order in condensed phases of silicon, Phys. Rev. B **31**, 5262 (1985).

[23] R. L. C. Vink, G. T. Barkema, W. F. van der Weg, and N. Mousseau, Fitting the stillinger–weber potential to amorphous silicon, J. Non-Cryst. Solids **282**, 248 (2001).

[24] See Supplemental Material at http://link.aps.org/supplemental/10.1103/PhysRevB.100.115307 for atomic-coordinate files ("ascii" files). The files are in plain ascii format and their content are self-explanatory. All coordinates are in angstrom unit and given in a Cartesian system. Besides the comment lines, the first two lines give the computer-box lattice parameters **a**, **b**, and **c** on the form a_x, b_x, b_y, c_x, c_y, and c_z, while $a_y = a_z = b_z = 0$. Then, the following lines give for each atom the coordinates x, y, z, and the element name.

[25] BIGDFT, version 1.8.

[26] S. Goedecker, M. Teter, and J. Hutter, Separable dual-space gaussian pseudopotentials, Phys. Rev. B **54**, 1703 (1996).

[27] C. Hartwigsen, S. Goedecker, and J. Hutter, Relativistic separable dual-space Gaussian pseudopotentials from H to Rn, Phys. Rev. B **58**, 3641 (1998).

[28] J. P. Perdew, K. Burke, and M. Ernzerhof, Generalized Gradient Approximation Made Simple, Phys. Rev. Lett. **77**, 3865 (1996).

[29] D. Levine and P. J. Steinhardt, Quasicrystals. I. definition and structure, Phys. Rev. B **34**, 596 (1986).

[30] A. Katz and M. Duneau, Quasiperiodic structures obtained by the projection method, J. Phys. Colloques **47**, C3-103 (1986).

[31] M. Torikai, K. Niizeki, and T. Odagaki, Binary self-similar one-dimensional quasilattices: Mutual local-derivability classification and substitution rules, J. Phys. Soc. Jpn. **70**, 2918 (2001).

[32] P. Bak, Icosahedral crystals from cuts in six-dimensional space, Scr. Metall. **20**, 1199 (1986).

[33] T. Janssen, Aperiodic crystals: A contradictio in terminis? Phys. Rep. **168**, 55 (1988).

[34] F. Lançon. and L. Billard, Binary tilings and quasi-quasicrystalline tilings, Phase Transitions **44**, 37 (1993).

[35] C. Godrèche and F. Lançon, A simple example of a non-Pisot tiling with five-fold symmetry, J. Phys. I France **2**, 207 (1992).

[36] C. Godrèche and J. M. Luck, Indexing the diffraction spectrum of a non-pisot self-similar structure, Phys. Rev. B **45**, 176 (1992).

[37] C. Sire, R. Mosseri, and J.-F. Sadoc, Geometric study of a 2D tiling related to the octagonal quasiperiodic tiling, J. Phys. France **50**, 3463 (1989).

[38] C. Sire, Electronic spectrum of a 2D quasi-crystal related to the octagonal quasi-periodic tiling, Europhys. Lett. **10**, 483 (1989).

[39] H. Q. Yuan, U. Grimm, P. Repetowicz, and M. Schreiber, Energy spectra, wave functions, and quantum diffusion for quasiperiodic systems, Phys. Rev. B **62**, 15569 (2000).

[40] W. Steurer and S. Deloudi, Tilings and coverings, in *Crystallography of Quasicrystals: Concepts, Methods and Structures* (Springer Berlin Heidelberg, Berlin, Heidelberg, 2009), pp. 7–47.

[41] L. Pizzagalli, J. Godet, J. Guénolé, S. Brochard, E. Holmstrom, K. Nordlund, and T. Albaret, A new parametrization of the stillinger-weber potential for an improved description of defects and plasticity of silicon, J. Phys.: Condens. Matter **25**, 055801 (2013).

[42] F. Lançon, Aubry transition in a real material: Prediction for its existence in an incommensurate gold/gold interface, Europhys. Lett. **57**, 74 (2002).

[43] F. Lançon, J.-M. Pénisson, and U. Dahmen, Quasicrystalline gold interface with a frictionless property, Europhys. Lett. **49**, 603 (2000).

[44] F. Lançon, J. Ye, D. Caliste, T. Radetic, A. M. Minor, and U. Dahmen, Superglide at an internal incommensurate boundary, Nano Lett. **10**, 695 (2010).

[45] S. Aubry, The new concept of transitions by breaking of analyticity in a crystallographic model, in *Solitons and Condensed Matter Physics*, edited by A. R. Bishop and T. Schneider, Solid-State Sciences Vol. 8 (Springer-Verlag, Berlin Heidelberg, 1978), pp. 264–277.

[46] P. Quémerais, Ground-states and growth structures for one-dimensional models with periodic to quasiperiodic transitions, in *Quasicrystals–Current Topics*, edited by E. Belin-Ferré, C. Berger, M. Quiquandon, and A. Sadoc (World Scientific, Singapore, 2000), pp. 187–211.

[47] J. E. Sacco and J. B. Sokoloff, Free sliding in lattices with two incommensurate periodicities, Phys. Rev. B **18**, 6549 (1978).

[48] M. Hirano and K. Shinjo, Atomistic locking and friction, Phys. Rev. B **41**, 11837 (1990).

[49] K. Shinjo and M. Hirano, Dynamics of friction: Superlubric state, Surf. Sci. **283**, 473 (1993).

[50] M. Cieplak, E. D. Smith, and M. O. Robbins, Molecular origins of friction: The force on adsorbed layers, Science **265**, 1209 (1994).

[51] M. Weiss and F.-J. Elmer, Dry friction in the Frenkel-Kontorova-Tomlinson model: Static properties, Phys. Rev. B **53**, 7539 (1996).

[52] M. R. Sørensen, K. W. Jacobsen, and P. Stoltze, Simulations of atomic-scale sliding friction, Phys. Rev. B **53**, 2101 (1996).

[53] M. Hirano, K. Shinjo, R. Kaneko, and Y. Murata, Observation of superlubricity by scanning tunneling microscopy, Phys. Rev. Lett. **78**, 1448 (1997).

[54] G. He, M. H. Müser, and M. O. Robbins, Adsorbed layers and the origin of static friction, Science **284**, 1650 (1999).

[55] M. H. Müser and M. O. Robbins, Conditions for static friction between flat crystalline surfaces, Phys. Rev. B **61**, 2335 (2000).

[56] J. S. Ko and A. J. Gellman, Friction anisotropy at Ni(100)/Ni(100) interfaces, Langmuir **16**, 8343 (2000).

[57] M. H. Müser, M. Urbakh, and M. O. Robbins, Statistical mechanics of static and low-velocity kinetic friction, in *Advances in Chemical Physics* (Wiley, Hoboken, NJ, 2003), Chap. 5, pp. 187–272.

[58] M. Dienwiebel, G. S. Verhoeven, N. Pradeep, J. W. M. Frenken, J. A. Heimberg, and H. W. Zandbergen, Superlubricity of Graphite, Phys. Rev. Lett. **92**, 126101 (2004).

[59] A. Socoliuc, R. Bennewitz, E. Gnecco, and E. Meyer, Transition from Stick-Slip to Continuous Sliding in Atomic Friction: Entering a New Regime of Ultralow Friction, Phys. Rev. Lett. **92**, 134301 (2004).

[60] *Superlubricity*, edited by A. Erdemir and J.-M. Martin (Elsevier Science, Amsterdam, Netherlands, 2007).

[61] T. Brazda, A. Silva, N. Manini, A. Vanossi, R. Guerra, E. Tosatti, and C. Bechinger, Experimental Observation of the Aubry Transition in Two-Dimensional Colloidal Monolayers, Phys. Rev. X **8**, 011050 (2018).

[62] S. Aubry, Devil's staircase and order without periodicity in classical condensed matter, J. Phys. France **44**, 147 (1983).

[63] S. Aubry, J.-P. Gosso, G. Abramovici, J.-L. Raimbault, and P. Quemerais, Effective discommensurations in the incommensurate ground states of the extended Frenkel-Kontorowa models, Physica D **47**, 461 (1991).